

Variable Eddington Factor Acceleration of Lumped Linear Discontinuous Galerkin/Mixed Finite Element Source Iteration

Samuel S. Olivier, Jim E. Morel

Department of Nuclear Engineering
Texas A&M University
College Station, TX 77843

Abstract

Insert abstract here

Keywords

Source Iteration acceleration, Lumped Linear Discontinuous Galerkin, Mixed Finite Element Method

Running Head

Variable Eddington Factor Method

Corresponding Author

Jim E. Morel, Phone: (979)845-6072, FAX: (979)845-6075, E-mail: *morel@tamu.edu*.

1 Introduction

The Variable Eddington Factor (VEF) method, also known as Quasi-Diffusion (QD), was one of the first nonlinear methods for accelerating source iterations in S_N calculations [1]. It is comparable in effectiveness to both linear and nonlinear forms of Diffusion-Synthetic Acceleration (DSA), but it offers much more flexibility than the DSA. Stability can only be guaranteed with DSA if the diffusion equation is differenced in a manner consistent with that of the S_N equations [2]. Modern S_N codes often use advanced discretization schemes such as discontinuous Galerkin (DG) since classic discretization schemes such as step and diamond are not suitable for radiative transfer calculations in the high-energy density laboratory physics (HEDLP) regime or coupled electron-photon calculations. Diffusion discretizations consistent with the DG S_N discretizations cannot actually be expressed in diffusion form, but rather must be expressed in first-order or P_1 form, and are much more difficult to solve than standard diffusion discretizations. Considerable effort has gone into the development of “partially consistent” diffusion discretizations that yield a stable DSA algorithm with some degree of degraded effectiveness, but such discretizations are also generally difficult to develop.

A great advantage of the VEF method is that the drift-diffusion equation that accelerates the S_N source iterations can be discretized in any valid manner without concern for consistency with the S_N discretization. When the VEF drift-diffusion equation is discretized in a way that is “non-consistent,” the S_N and VEF drift-diffusion solutions for the scalar flux do not necessarily become identical when the iterative process converges. However, they do become identical in the limit as the spatial mesh is refined, and the difference between the two solutions is proportional to the spatial truncation errors associated with the S_N and drift-diffusion discretizations. In general the order of accuracy of the S_N and VEF drift-diffusion

solutions will be the lowest order accuracy of their respective independent discretizations. Although the S_N solution obtained with such a “non-consistent” VEF method is not conservative, the VEF drift-diffusion solution is in fact conservative. This is particularly useful in multiphysics calculations where the low-order VEF equation can be coupled to the other physics components rather than the high-order S_N equations. Another advantage of the non-consistent approach is that even if the S_N spatial discretization scheme does not preserve the thick diffusion limit [1], that limit will generally be preserved using the VEF method.

The purpose of this paper is to investigate the application of the VEF method with the 1-D S_N equations discretized with the lumped linear-discontinuous method (LLDG) and the drift-diffusion equation discretized using the constant-linear mixed finite-element method (MFEM). To our knowledge, this combination has not been previously investigated. Our motivation for this investigation is that MFEM methods are now being used for high-order hydrodynamics calculations at Lawrence Livermore National Laboratory [2]. A radiation transport method compatible with MFEM methods is clearly desirable for developing a MFEM radiation-hydrodynamics code. Such a code would combine thermal radiation transport with hydrodynamics. However, MFEM methods are inappropriate for the first-order form of the transport equation, and are problematic even for the even-parity form. [3]. Thus the use of the VEF method with a DG S_N discretization and a MFEM drift-diffusion discretization suggests itself. Here we define a VEF method that should exhibit second-order accuracy since both the transport and drift-diffusion discretizations are second-order accurate in isolation. In addition, our VEF method should preserve the thick diffusion limit [1], which is essential for radiative transfer calculations in the HEDLP regime. We use the lumped rather than the standard LDG discretization because lumping yields a much more robust scheme, and robustness is essential for radiative transfer calculations in the HEDLP

regime. Because this is an initial study, we simplify the investigation by considering only one-group neutron transport rather than the full radiative transfer equations, which include a material temperature equation as well as the radiation transport equation. The vast majority of relevant properties of a VEF method for radiative transfer can be tested with an analogous method for one-group neutron transport. Furthermore, a high-order DG-MFEM VEF method could be of interest for neutronics in addition to radiative transfer calculations. A full investigation for radiative transfer calculations will be carried out in a future study.

The remainder of this paper is organized as follows. First, we describe the VEF method analytically. Then we describe our discretized S_N equations, followed by a description of the discretized VEF drift-diffusion equation. We next give computational results. More specifically, we describe two ways to represent the S_N variable Eddington factor in the MFEM drift-diffusion equation and several ways to construct the S_N scattering source from the drift-diffusion solution for the scalar flux. Each of these options yields a different VEF method. The accuracy of these methods is then compared to that of the standard lumped LDG S_N solution for several test problems, and the iterative convergence rate of these methods is compared to that of the lumped LDG S_N equations with fully-consistent S_2 Synthetic Acceleration (S_2SA). Finally, we give conclusions and recommendations for future work.

2 The VEF Method

2.1 The Algorithm

Here, we describe the VEF method for a planar geometry, fixed-source problem:

$$\mu \frac{\partial \psi}{\partial x}(x, \mu) + \sigma_t(x) \psi(x, \mu) = \frac{\sigma_s(x)}{2} \int_{-1}^1 \psi(x, \mu') d\mu' + \frac{Q(x)}{2}, \quad (1)$$

where $\mu = \cos \theta$ is the cosine of the angle of flight θ relative to the x -axis, $\sigma_t(x)$ and $\sigma_s(x)$ the total and scattering macroscopic cross sections, $Q(x)$ the isotropic fixed-source and $\psi(x, \mu)$ the angular flux. Applying the Discrete Ordinates (S_N) angular discretization yields the following set of N coupled, ordinary differential equations:

$$\mu_n \frac{d\psi_n}{dx}(x) + \sigma_t(x)\psi_n(x) = \frac{\sigma_s(x)}{2}\phi(x) + \frac{Q(x)}{2}, 1 \leq n \leq N, \quad (2)$$

where $\psi_n(x) = \psi(x, \mu_n)$ is the angular flux in direction μ_n . The μ_n are stipulated by an N -point Gauss quadrature rule such that the scalar flux, $\phi(x)$, can be numerically integrated with:

$$\phi(x) = \sum_{n=1}^N w_n \psi_n(x), \quad (3)$$

where the w_n are the quadrature weights corresponding to the μ_n .

The VEF method decouples Eq. 2 by lagging the scattering term:

$$\mu_n \frac{d\psi_n^{\ell+1/2}}{dx}(x) + \sigma_t(x)\psi_n^{\ell+1/2}(x) = \frac{\sigma_s(x)}{2}\phi^\ell(x) + \frac{Q(x)}{2}, 1 \leq n \leq N, \quad (4)$$

where the superscripts indicate the iteration index. In Source Iteration (SI), the update

$$\phi(x)^{\ell+1} = \phi(x)^{\ell+1/2} \quad (5)$$

is used. However, this is slow to converge in optically thick and highly scattering systems. Instead, the VEF method solves the VEF drift diffusion equations found by taking the first two angular moments of Eq. 2:

$$\frac{d}{dx}J^{\ell+1}(x) + \sigma_a(x)\phi^{\ell+1}(x) = Q(x), \quad (6a)$$

$$\frac{d}{dx} \langle \mu^2 \rangle^{\ell+1/2}(x) \phi^{\ell+1}(x) + \sigma_t(x) J^{\ell+1}(x) = 0, \quad (6b)$$

where $J^{\ell+1}(x)$ is the current and

$$\langle \mu^2 \rangle^{\ell+1/2}(x) = \frac{\int_{-1}^1 \mu^2 \psi^{\ell+1/2}(x, \mu) d\mu}{\int_{-1}^1 \psi^{\ell+1/2}(x, \mu) d\mu} \xrightarrow{S_N} \frac{\sum_{n=1}^N \mu_n^2 \psi_n^{\ell+1/2}(x) w_n}{\sum_{n=1}^N \psi_n^{\ell+1/2}(x) w_n} \quad (7)$$

the Eddington factor. The scattering term in Eq. 4 is then updated with the VEF drift diffusion scalar flux found by solving Eqs. 6a and 6b. This process of solving Eq. 4 for the $\psi_n(x)$, computing the Eddington factor, solving the VEF drift diffusion equation for the scalar flux, and updating the scattering term with the VEF drift diffusion scalar flux is repeated convergence.

Acceleration occurs because the angular shape of the angular flux, and thus the Eddington factor, converges much faster than the scalar flux. In addition, the VEF equations model the contributions of all scattering events at once, reducing the dependence on source iterations to introduce scattering information.

In addition to acceleration, this scheme allows the S_N equations and drift diffusion equations to be solved with arbitrarily different spatial discretization methods. The following sections present the application of the Lumped Linear Discontinuous Galerkin (LLDG) spatial discretization to the S_N equations and the Mixed Finite Element Method (MFEM) to the VEF drift diffusion equations.

2.2 Lumped Linear Discontinuous Galerkin S_N

The LLDG discretization of Eq. 4 is:

$$\mu_n \left(\psi_{n,i}^{\ell+1/2} - \psi_{n,i-1/2}^{\ell+1/2} \right) + \frac{\sigma_{t,i} h_i}{2} \psi_{n,i,L}^{\ell+1/2} = \frac{\sigma_{s,i} h_i}{4} \phi_{i,L}^{\ell} + \frac{h_i}{4} Q_{i,L}, \quad (8a)$$

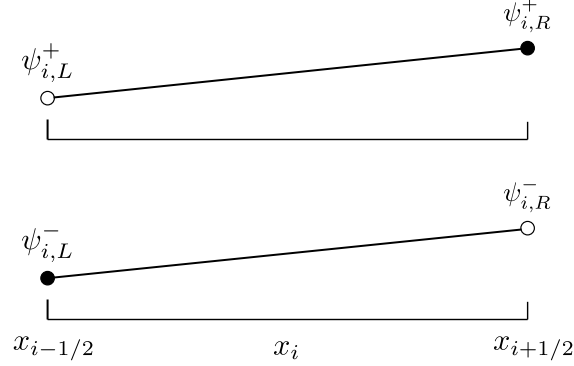


Figure 1: The distribution of unknowns in an LLDG cell. The superscript $+$ and $-$ indicate the angular fluxes for $\mu_n > 0$ and $\mu_n < 0$, respectively.

$$\mu_n \left(\psi_{n,i+1/2}^{\ell+1/2} - \psi_{n,i}^{\ell+1/2} \right) + \frac{\sigma_{t,i} h_i}{2} \psi_{n,i,R}^{\ell+1/2} = \frac{\sigma_{s,i} h_i}{4} \phi_{i,R}^{\ell} + \frac{h_i}{4} Q_{i,R}, \quad (8b)$$

where h_i , $\sigma_{t,i}$, and $\sigma_{s,i}$ are the cell width, total cross section, and scattering cross section in cell i . The i, L and i, R subscripts indicate the the subscripted value is the left or right discontinuous edge value. The cell centered angular flux is the average of the left and right discontinuous edge fluxes:

$$\psi_{n,i}^{\ell+1/2} = \frac{1}{2} \left(\psi_{n,i,L}^{\ell+1/2} + \psi_{n,i,R}^{\ell+1/2} \right). \quad (9)$$

The cell edged angular fluxes are defined through upwinding:

$$\psi_{n,i-1/2}^{\ell+1/2} = \begin{cases} \psi_{n,i-1,R}^{\ell+1/2}, & \mu_n > 0 \\ \psi_{n,i,L}^{\ell+1/2}, & \mu_n < 0 \end{cases}, \quad (10a)$$

$$\psi_{n,i+1/2}^{\ell+1/2} = \begin{cases} \psi_{n,i,R}^{\ell+1/2}, & \mu_n > 0 \\ \psi_{n,i+1,L}^{\ell+1/2}, & \mu_n < 0 \end{cases}. \quad (10b)$$

Equations 8a, 8b, 9, 10a, and 10b can be combined and rewritten as

$$\begin{bmatrix} \mu_n + \sigma_{t,i} h_i & \mu_n \\ -\mu_n & \sigma_{t,i} + \mu_n \end{bmatrix} \begin{bmatrix} \psi_{n,i,L}^{\ell+1/2} \\ \psi_{n,i,R}^{\ell+1/2} \end{bmatrix} = \begin{bmatrix} \frac{\sigma_{s,i} h_i}{2} \phi_{i,L}^{\ell} + \frac{h_i}{2} Q_{i,L} + 2\mu_n \psi_{n,i-1,R}^{\ell+1/2} \\ \frac{\sigma_{s,i} h_i}{2} \phi_{i,R}^{\ell} + \frac{h_i}{2} Q_{i,R} \end{bmatrix}, \quad (11)$$

for sweeping from left to right ($\mu_n > 0$) and

$$\begin{bmatrix} -\mu_n + \sigma_{t,i} h_i & \mu_n \\ -\mu_n & -\mu_n + \sigma_{t,i} h_i \end{bmatrix} \begin{bmatrix} \psi_{n,i,L}^{\ell+1/2} \\ \psi_{n,i,R}^{\ell+1/2} \end{bmatrix} = \begin{bmatrix} \frac{\sigma_{s,i} h_i}{2} \phi_{i,L}^{\ell} + \frac{h_i}{2} Q_{i,L} \\ \frac{\sigma_{s,i} h_i}{2} \phi_{i,R}^{\ell} + \frac{h_i}{2} Q_{i,R} - 2\mu_n \psi_{n,i+1,L}^{\ell+1/2} \end{bmatrix}, \quad (12)$$

for sweeping from right to left ($\mu_n < 0$). The right hand sides of Eqs. 11 and 12 are known as the scalar flux from the previous iteration, the fixed source, and the angular flux entering from the previous cell are all known. By supplying the flux entering the left side of the first cell, the positive-angled solution can be propagated from left to right by solving Eq. 11. Similarly, supplying the incident flux on the right boundary allows the negative-angled solution to be propagated from right to left with Eq. 12.

2.3 Mixed Finite Element Method VEF Drift Diffusion

The unknowns in an MFEM cell are depicted in Fig. 2. The scalar flux is constant within the cell with discontinuous jumps at the cell edges and the current is a linear function defined by:

$$J_i(x) = J_{i,L} B_{i,L}(x) + J_{i,R} B_{i,R}(x), \quad (13)$$

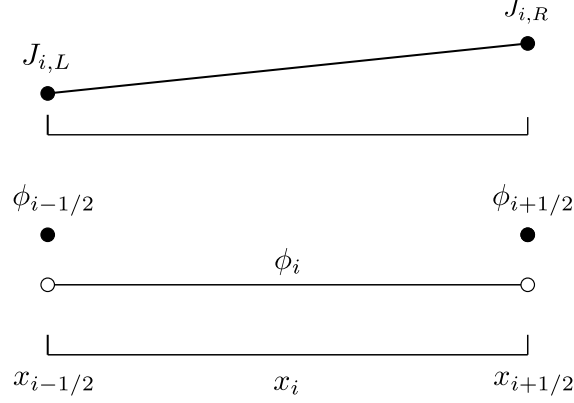


Figure 2: The distribution of unknowns in cell i for MFEM.

where $J_{i,L/R}$ are the currents at the left and right edges of the cell and

$$B_{i,L}(x) = \begin{cases} \frac{x_{i+1/2}-x}{h_i}, & x \in [x_{i-1/2}, x_{i+1/2}] \\ 0, & \text{otherwise} \end{cases}, \quad (14a)$$

$$B_{i,R}(x) = \begin{cases} \frac{x-x_{i-1/2}}{h_i}, & x \in [x_{i-1/2}, x_{i+1/2}] \\ 0, & \text{otherwise} \end{cases}, \quad (14b)$$

are the MFEM basis functions.

The spatial grid used in the MFEM VEF step is identical to the grid used in the LLDG S_N discretization. Overlap between the methods occurs in transferring the Eddington factor from LLDG S_N to MFEM VEF drift diffusion. MFEM requires the Eddington factor on the cell edges and cell centers. The edge values of the Eddington factor can be found by using the edge angular flux defined in Eqs. 10a and 10b. Two methods have been tested for the cell centers. The first method averages the edge Eddington factors and the second represents

the LLDG angular flux as a linear function of the MFEM basis functions:

$$\langle \mu^2 \rangle_i(x) = \frac{\sum_{n=1}^N \mu_n^2 [\psi_{n,i,L} B_{i,L}(x) + \psi_{n,i,R} B_{i,R}(x)]}{B_{i,L}(x) \sum_{n=1}^N w_n \psi_{n,i,L} + B_{i,R}(x) \sum_{n=1}^N w_n \psi_{n,i,R}}. \quad (15)$$

The MFEM representation yields five unknowns per cell: $\phi_{i-1/2}$, ϕ_i , $\phi_{i+1/2}$, $J_{i,L}$, and $J_{i,R}$. An equation for ϕ_i is found by integrating Eq. 6a over cell i :

$$J_{i,R} - J_{i,L} + \sigma_{a,i} h_i \phi_i = Q_i h_i, \quad (16)$$

where $\sigma_{a,i}$ and Q_i are the absorption cross section and source in cell i . Equations for $J_{i,L/R}$ are found by multiplying Eq. 6b by $B_{i,L/R}$ and integrating over cell i :

$$-\langle \mu^2 \rangle_{i-1/2} \phi_{i-1/2} + \langle \mu^2 \rangle_i \phi_i + \sigma_{t,i} h_i \left(\frac{1}{3} J_{i,L} + \frac{1}{6} J_{i,R} \right) = 0, \quad (17a)$$

$$\langle \mu^2 \rangle_{i+1/2} \phi_{i+1/2} - \langle \mu^2 \rangle_i \phi_i + \sigma_{t,i} h_i \left(\frac{1}{6} J_{i,L} + \frac{1}{3} J_{i,R} \right) = 0, \quad (17b)$$

where the Eddington factor is evaluated at iteration $\ell + 1/2$ and the fixed source has been assumed to be isotropic. The cell centered Eddington factor given in Eq. 15 is a rational polynomial and cannot be integrated analytically. In this case, two point Gauss quadrature was used to numerically integrate Eq. 15 over the interior of cell i :

$$\langle \mu^2 \rangle_i = \frac{1}{2} [\langle \mu^2 \rangle_i(x_{i,L}) + \langle \mu^2 \rangle_i(x_{i,R})], \quad (18)$$

where

$$x_{i,L/R} = \frac{h_i}{2} \mp \frac{x_{i+1/2} + x_{i-1/2}}{2\sqrt{3}} \quad (19)$$

are the quadrature points in the cell. Eliminating $J_{i,R}$ and $J_{i,L}$ yields:

$$J_{i,L} = \frac{-2}{\sigma_{t,i}h_i} \left\{ 2 [\langle \mu^2 \rangle_i \phi_i - \langle \mu^2 \rangle_{i-1/2} \phi_{i-1/2}] - [\langle \mu^2 \rangle_{i+1/2} \phi_{i+1/2} - \langle \mu^2 \rangle_i \phi_i] \right\}, \quad (20a)$$

$$J_{i,R} = \frac{-2}{\sigma_{t,i}h_i} \left\{ 2 [\langle \mu^2 \rangle_{i+1/2} \phi_{i+1/2} - \langle \mu^2 \rangle_i \phi_i] - [\langle \mu^2 \rangle_i \phi_i - \langle \mu^2 \rangle_{i-1/2} \phi_{i-1/2}] \right\}. \quad (20b)$$

The fourth equation is found by enforcing continuity of current:

$$J_{i,R} = J_{i+1,L}. \quad (21)$$

Using the definitions of $J_{i,L}$ and $J_{i,R}$ from Eqs. 20a and 20b in the balance equation (Eq. 16) and continuity equation (Eq. 21) reduces the system to three unknowns per cell: $\phi_{i-1/2}$, ϕ_i , and $\phi_{i+1/2}$. The resulting equations for ϕ_i and $\phi_{i+1/2}$ are:

$$-\frac{6}{\sigma_{t,i}h_i} \langle \mu^2 \rangle_{i-1/2} \phi_{i-1/2} + \left(\frac{12}{\sigma_{t,i}h_i} \langle \mu^2 \rangle_i + \sigma_{a,i}h_i \right) \phi_i - \frac{6}{\sigma_{t,i}h_i} \langle \mu^2 \rangle_{i+1/2} \phi_{i+1/2} = Q_i h_i, \quad (22a)$$

$$\begin{aligned} -\frac{2}{\sigma_{t,i}h_i} \langle \mu^2 \rangle_{i-1/2} \phi_{i-1/2} + \frac{6}{\sigma_{t,i}h_i} \langle \mu^2 \rangle_i \phi_i - 4 \left(\frac{1}{\sigma_{t,i}h_i} + \frac{1}{\sigma_{t,i+1}h_{i+1}} \right) \langle \mu^2 \rangle_{i+1/2} \phi_{i+1/2} \\ + \frac{6}{\sigma_{t,i+1}h_{i+1}} \langle \mu^2 \rangle_{i+1} \phi_{i+1} - \frac{2}{\sigma_{t,i+1}h_{i+1}} \langle \mu^2 \rangle_{i+3/2} \phi_{i+3/2} = 0. \end{aligned} \quad (22b)$$

On the interior, $\phi_{i-1/2} = \phi_{(i-1)+1/2}$. Thus, Eqs. 22a and 22b are sufficient to specify the center and edge scalar fluxes on the interior. The remaining unknowns, $\phi_{1/2}$ and $\phi_{I+1/2}$, are set by the boundary conditions. Equations for $\phi_{1/2}$ and $\phi_{I+1/2}$ are found by setting the $J_{1,L}$ and $J_{I,R}$ to a supplied boundary current. For example, a vacuum condition can be applied

on the left boundary through a modified Marshak boundary:

$$J_{1,L} = B_{1/2}\phi_{1/2} , \quad (23)$$

where $J_{1,L}$ is defined in Eq. 20a and

$$B_{1/2} = \frac{\sum_{n=1}^N |\mu_n| \psi_{n,1/2} w_n}{\sum_{n=1}^N \psi_{n,1/2} w_n} . \quad (24)$$

A left reflecting condition is set by

$$J_{1,L} = 0 . \quad (25)$$

This system of $2I + 1$ equations was assembled into a matrix with both cell centered and cell edge scalar fluxes and solved with a five band matrix solver.

Once the MFEM scalar flux has been found, the LLDG scattering term must be reconstructed. Two methods have been tested: no reconstruction and van Leer limited cell centered slope reconstruction. The no reconstruction method sets the LLDG discontinuous left and right scalar flux to the MFEM edge scalar flux:

$$\phi_{i,L/R} = \phi_{i\mp 1/2} , \quad (26)$$

where the left hand side is the reconstructed LLDG flux used in the scattering term of Eq. 4 and the right hand side the MFEM drift diffusion flux. The van Leer cell centered reconstruction is:

$$\phi_{i,L/R} = \phi_i \mp \frac{1}{4} \xi_{\text{van Leer}} [(\phi_{i+1} - \phi_i) + (\phi_i - \phi_{i-1})] , \quad (27)$$

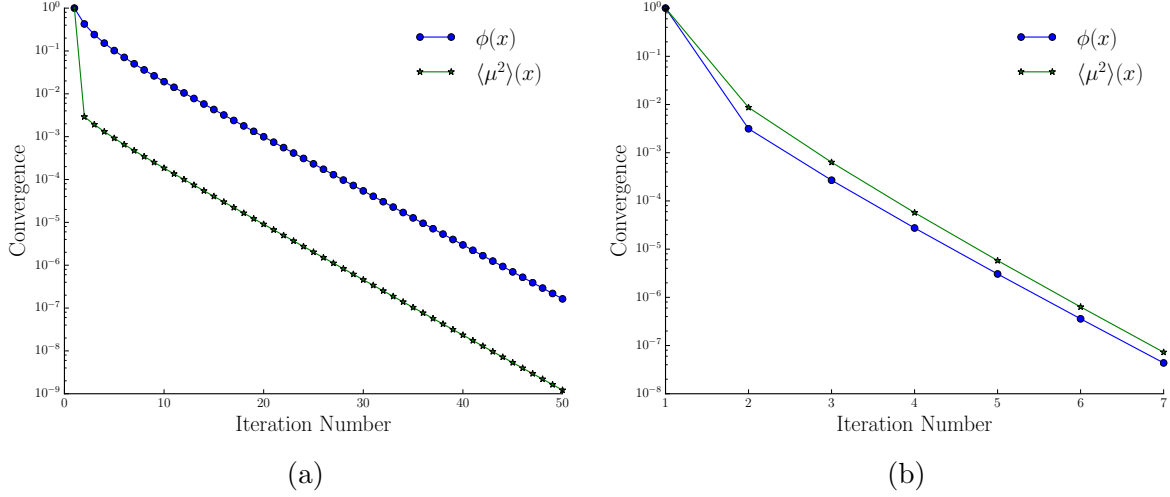


Figure 3: The convergence rate for $\phi(x)$ and $\langle \mu^2 \rangle(x)$ for (a) unaccelerated and (b) VEF accelerated SI.

where $\xi_{\text{van Leer}}$ the slope limiter given in [1].

3 Computational Results

Figure 3a shows the convergence criterion

$$\frac{\|f^{\ell+1} - f^\ell\|}{\|f^{\ell+1}\|} \quad (28)$$

as a function of unaccelerated iteration number for $f = \phi(x)$ and $f = \langle \mu^2 \rangle(x)$. The large drop in the convergence criterion between the first and second iterations supports the claim that the angular shape of the angular flux, and thus the Eddington factor, converges rapidly. When compared to Fig. 3b, a plot of the convergence criterion versus number of iterations for the VEF method, it is clear that the VEF method transfers the fast rate of convergence of the Eddington factor to the scalar flux.

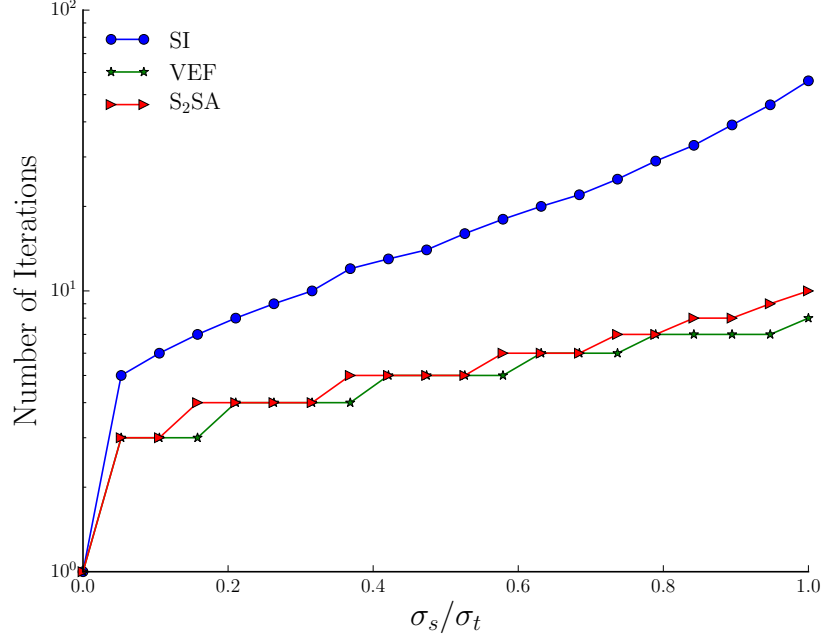


Figure 4: A comparison of the number of iterations required for Source Iteration, VEF acceleration, and S₂SA to converge for varying ratios of σ_s to σ_t .

To compare SI, VEF, and consistently differenced S₂SA, a test problem with a reflecting left boundary and a vacuum right boundary was used. This system was discretized into 50 spatial cells. σ_t was set to 1 cm^{-1} leading to an optical thickness per cell of 0.2. The convergence tolerance was set to 10^{-6} . Figure 4 shows the number of iterations required for convergence for SI, VEF, and S₂SA for varying ratios of σ_s to σ_t . Aside from $\sigma_s/\sigma_t = 0$ where acceleration is not possible, the ratio of unaccelerated to VEF accelerated iterations ranged from 1.6 to 7. This suggests that acceleration is occurring and that the VEF method is not just doing twice the amount of work per iteration. In addition, the VEF method performed similarly to S₂SA.

The Method of Manufactured Solutions (MMS) was used to compare the accuracy of the VEF method as the cell width was decreased. The L2 norm of the difference between

Reconstruction Method	ψ Representation	Order	C	R^2
None	Constant	1.997	0.682	9.9999×10^{-1}
None	Linear	1.998	0.687	1.0000
Center	Constant	2.007	0.726	9.9992×10^{-1}
Center	Linear	2.009	0.732	9.9991×10^{-1}

Table 1: The order of accuracy, error, and R^2 values for the permutations of the two Ed-dington representation methods and two slope reconstruction methods.

the numerical and MMS solutions was compared at five logarithmically spaced cell widths between 0.5 mm and 0.01 mm. A line of best fit of the form

$$E = Ch^n \quad (29)$$

was used to find the order of accuracy, n , and the constant of proportionality, C , of the numerical error, E . These values are provided in Table 1 for the permutations of the two reconstruction methods and two angular flux representation methods. All of the permutations are second order accurate and have similar overall accuracy. This suggests that slope reconstruction and angular flux representation do not affect numerical accuracy. It is also a testament to the robustness of the VEF method as the inconsistent, partially consistent, and fully consistent methods all performed similarly.

The convergence between unaccelerated SI and the VEF method was compared as a function of cell width for a simple homogeneous slab and for Reed’s problem. In both cases, the left boundary was reflecting and the right boundary was vacuum. The homogeneous slab had a scattering ratio of 0.75. The cross sections and source for Reed’s problem are provided in Table 2. The L2 norm of the difference between the SI solution and VEF solution is plotted for the four permutations of no reconstruction, van Leer slope limited reconstruction, constant angular flux representation, and linear angular flux representation

	Region 1	Region 2	Region 3	Region 4	Region 5
q	50	0	0	0	1
Σ_t	50	0.001	1	5	1
Σ_a	50	0	0.1	0	0.1
Domain	$0 \leq x < 2$	$2 \leq x < 4$	$4 \leq x < 6$	$6 \leq x < 7$	$7 \leq x \leq 8$

Table 2: The cross sections and source used for Reed’s problem.

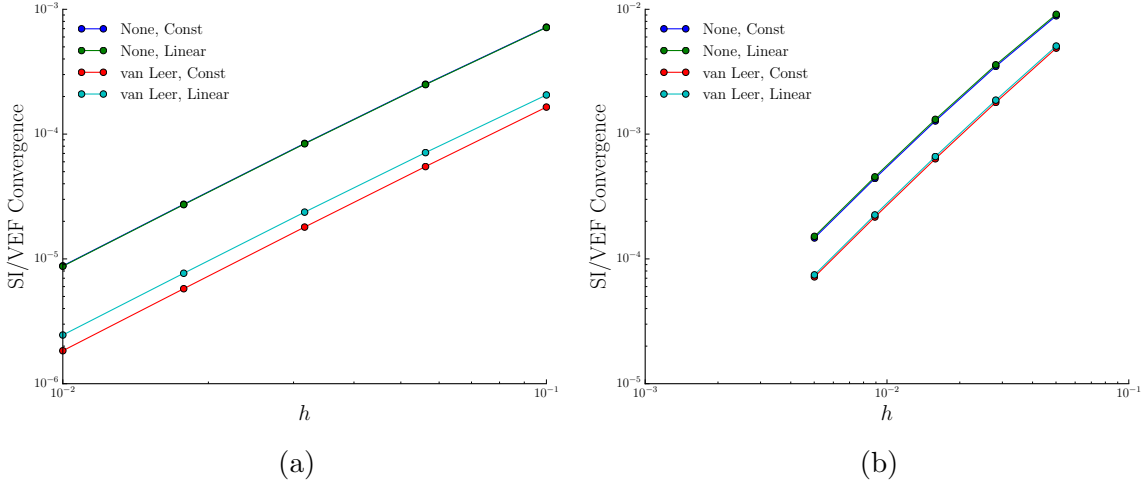


Figure 5: The L2 norm of the difference between SI and the four permutations of the VEF method as the cell spacing is decreased for (a) the homogeneous slab problem and (b) Reed’s problem.

in Figures 5a and 5b for the homogeneous slab problem and Reed’s problem.

In the homogeneous problem, VEF with van Leer limited slope reconstruction was five times more convergent than VEF without reconstruction. Use of the linear angular flux representation decreased the van Leer reconstruction convergence by 30%. In Reed’s problem, all four methods performed similarly. This suggests that the effects of an angular flux representation and slope reconstruction are problem dependent.

Lastly, slope reconstruction and angular flux representation were tested in the diffusion

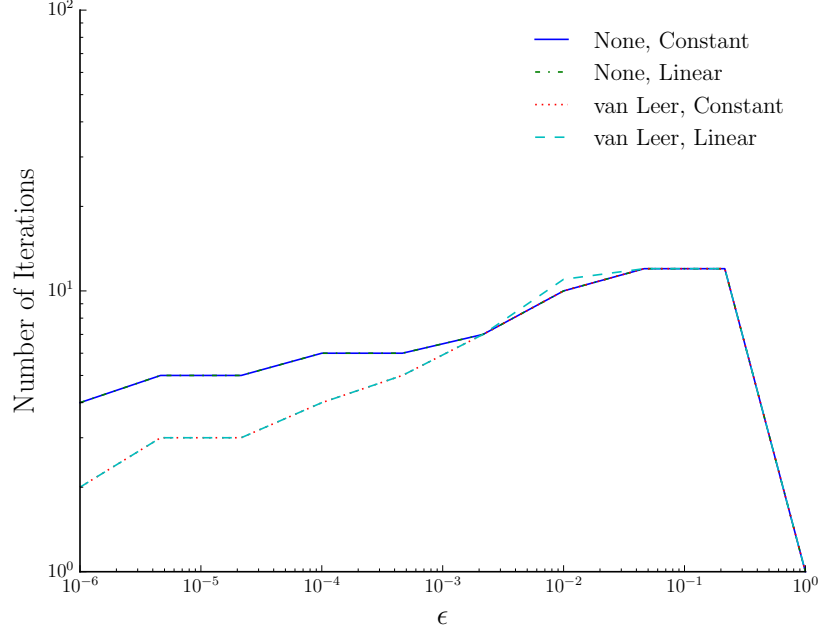


Figure 6: The number of iterations required for convergence for the permutations of slope reconstruction and angular flux representation in the diffusion limit.

limit. The cross sections and source were scaled according to:

$$\sigma_t(x) \rightarrow \sigma_t(x)/\epsilon, \quad (30a)$$

$$\sigma_s(x) \rightarrow \epsilon\sigma_s(x), \quad (30b)$$

$$Q(x) \rightarrow \epsilon Q(x). \quad (30c)$$

As $\epsilon \rightarrow 0$, the system becomes diffusive. The number of iterations for convergence within a tolerance of 10^{-10} as $\epsilon \rightarrow 0$ is plotted in Fig. 6. The error between the VEF solution and the exact diffusion solution is provided in Fig. 7. This supports the claim that the VEF method is robust as all four permutations survived the diffusion limit.

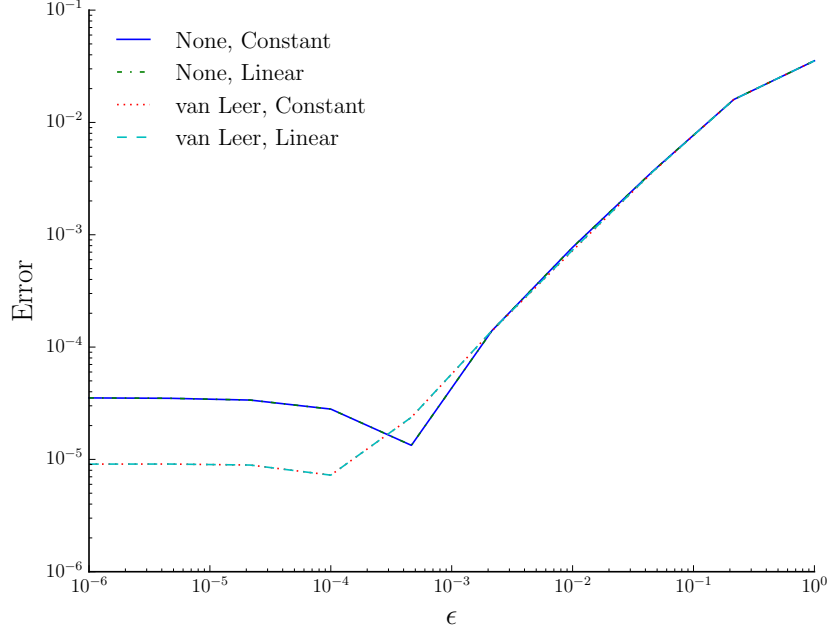


Figure 7: The error between the VEF methods and the exact diffusion solution as $\epsilon \rightarrow 0$.

4 Conclusions and Future Work

We have presented the VEF method for one-group neutron transport in slab geometry and the pairing of LLDG for the S_N transport step and MFEM for the drift diffusion acceleration step. We have numerically demonstrated that the LLDG/MFEM VEF method accelerates Source Iteration by transferring the rapid convergence of the angular shape of the angular flux to the scalar flux. The VEF method performed similarly to consistently differenced S_2SA .

Methods for increased consistency between LLDG and MFEM were also presented. This included a cell centered slope reconstruction method that will be needed for radiative transfer calculations. It was shown that the inconsistent, partially consistent, and fully consistent methods were second-order accurate as expected from the orders of accuracy of LLDG and

MFEM in isolation and that all of the VEF methods were robust in the diffusion limit. In addition, while this nonlinear scheme produces two solutions, one from S_N and one from drift diffusion, the solutions were shown to converge as the mesh was refined for both homogeneous and inhomogeneous systems.

Future work includes extending the VEF method presented in this paper to the radiative transfer equations and verifying the VEF method in 2 and 3 dimensional systems.

References

- [1] B. van Leer. Towards the ultimate conservative difference scheme I: The quest for monotonicity. *Lecture Notes in Physics*, 18:163–168, 1973.